AGU PUBLICATIONS

Geochemistry, Geophysics, Geosystems

RESEARCH ARTICLE
10.1002/2015GC006092

Key Points:
- Maximum horizontal principal stress (S_{Hmax}) orientations were observed in three drill sites
- S_{Hmax} at the base of a mid-slope site is oriented in the plate convergence direction
- S_{Hmax} directions elsewhere in the sediment cover are variable and likely controlled by normal faulting

Supporting Information:
- Supporting Information S1
- Table S1
- Table S2
- Table S3

Correspondence to:
A. Malinverno,
alberto@ldeo.columbia.edu

Citation:
Malinverno, A., S. Saito, and P. Vannucchi (2016), Horizontal principal stress orientation in the Costa Rica Seismogenesis Project (CRISP) transect from borehole breakouts, *Geochem. Geophys. Geosyst.*, *17*, 65–77, doi:10.1002/2015GC006092.

Received 9 SEP 2015
Accepted 10 DEC 2015
Accepted article online 15 DEC 2015
Published online 14 JAN 2016

Horizontal principal stress orientation in the Costa Rica Seismogenesis Project (CRISP) transect from borehole breakouts

A. Malinverno[1], S. Saito[2], and P. Vannucchi[3]

[1]Lamont-Doherty Earth Observatory, Columbia University, Palisades, New York, USA, [2]Institute for Research on Earth Evolution, Japan Agency for Marine-Earth Science and Technology, Yokosuka, Japan, [3]Department of Earth Sciences, Royal Holloway, University of London, Egham, UK

Abstract The Costa Rica Seismogenesis Project (CRISP) drilled the Pacific margin of the Middle America Trench just north of where the Cocos Ridge enters the subduction zone, resulting in basal erosion of the upper plate. Here we report the orientations of the maximum horizontal principal stress (S_{Hmax}) from borehole breakouts detected by logging-while-drilling and wireline downhole measurements. All S_{Hmax} directions were estimated in the sediment cover of the margin, above the deeper rocks of the deformed margin wedge. We observe three overall S_{Hmax} orientations: NNE-SSW (25° azimuth) in the deepest interval drilled at the upper slope Site U1379; ENE-WSW (82°) in the rest of Site U1379 and in Site U1413, also drilled in the upper slope; and NNW-SSE (157°) in the mid-slope Site U1378. Our preferred interpretation is that the deepest interval of Site U1379 records the stress conditions in the underlying margin wedge, as S_{Hmax} is parallel to the direction of the Cocos-Caribbean plate convergence and of the compressional axes of plate boundary fault earthquakes. The variable S_{Hmax} directions observed elsewhere are likely due to the effect of a network of normal faults that subdivide the sediment cover into a number of independently deforming blocks. In addition, the observed S_{Hmax} directions may be influenced by the subducting Cocos Ridge, which acts as an indenter causing oblique deformation, and by the transition to seismogenic subduction along the plate boundary fault.

1. Introduction

Subduction at convergent plate margins is a key process in global plate tectonics. Part of the subducted lithosphere is recycled into the mantle, while magmas generated by partial melting result in intense volcanic activity and create new continental crust. Subduction at convergent margins also produces the most powerful and deepest earthquakes on Earth. There are two end-member types of convergent margins, accretionary and erosive [*von Huene and Scholl*, 1991; *Clift and Vannucchi*, 2004]. Accretionary margins are typically found where plate convergence is slow and the underthrusting plate has a relatively thick sediment cover. At the leading edge of the upper plate, these margins contain a prominent accretionary wedge that grows over time by incorporating some of the sediments from the underthrusting, lower plate. In contrast, at erosive margins, the upper plate progressively shrinks as its base loses material to the subduction zone. Erosive margins are generally found where plate convergence is fast and the sediment cover on the underthrusting plate is thin [*Clift and Vannucchi*, 2004].

The results presented here were obtained during Integrated Ocean Drilling Program Expeditions 334 and 344 of the Costa Rica Seismogenesis Project [*Vannucchi et al.*, 2012; *Harris et al.*, 2013]. The CRISP transect is located at the southern end of the Middle America Trench where the Cocos plate is being subducted beneath the Caribbean plate just north of the Cocos Ridge axis (Figure 1). This location was chosen as an erosive type margin because the subduction of the Cocos Ridge results in a relatively shallow plate boundary fault that makes the upper end of the seismogenic zone accessible to deep riser drilling. In addition to the coring and logging results obtained during the initial phase of CRISP, a 3-D seismic survey has been recently acquired [*Bangs et al.*, 2015]. The CRISP project complements the Nankai Trough Seismogenic Zone Experiment (NanTroSEIZE), whose ultimate objective is to drill the seismogenic zone in an accretionary convergent margin [*Tobin et al.*, 2014].

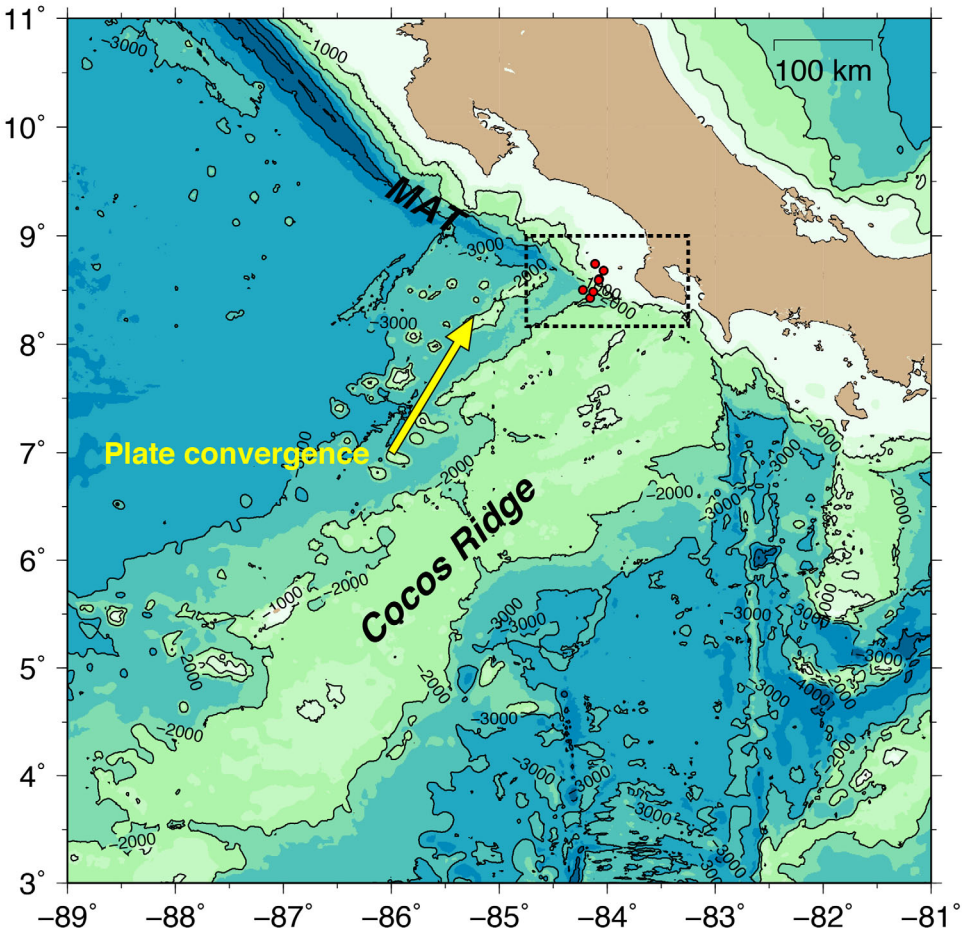

Figure 1. Location of the CRISP sites (dots) on the Costa Rica Pacific margin. The dotted line is the area in the detailed map in Figure 2, and the yellow arrow indicates the Cocos-Caribbean plate relative motion. MAT = Middle America Trench. Contour interval is 1000 m. The plot was generated with the Generic Mapping Tools (GMT) package [*Wessel et al.*, 2013].

Here we report the present orientations of the maximum horizontal principal stress inferred from downhole measurements of borehole breakouts in three sites drilled during the CRISP expeditions (Figures 1–3). The state of stress in the overriding plate controls deformation and faulting, is a function of the coupling at the plate boundary, and can change during the earthquake cycle [*Wang and Hu*, 2006; *Wang et al.*, 2010]. A global survey of lithospheric stress orientation shows that the large-scale, first-order patterns of horizontal principal stress directions are controlled by compressional forces applied at plate boundaries [*Zoback*, 1992]. Results obtained from borehole breakout analyses in holes drilled on the accretionary Nankai margin sites generally show a maximum horizontal stress direction nearly parallel to the plate convergence, with the exception of a site in the fore-arc basin where the stress state denotes margin-perpendicular extension [*Chang et al.*, 2010; *Lin et al.*, 2010]. Our results complement the global database of present-day maximum horizontal principal stress directions [*Heidbach et al.*, 2009] with measurements in the upper plate of an erosive convergent margin.

2. Background

The CRISP drilling area is located above the subducting northwest flank of the NE-SW trending aseismic Cocos Ridge (Figures 1 and 2), which consists of thickened oceanic crust produced by Galapagos magmatism and has a relief of 2.5 km over the adjacent ocean floor [*Walther*, 2003]. The subduction of the Cocos Ridge produces basal erosion seaward of the Osa peninsula [*Vannucchi et al.*, 2013]. The Cocos Ridge also acts as an indenter, as shown by the fanning pattern of deformation away from the Cocos Ridge axis measured by GPS [*LaFemina et al.*, 2009; *Kobayashi et al.*, 2014]. The Osa peninsula lies on top of the subducted Cocos Ridge axis and its geology suggests that the bulk of the overriding plate there is a Cenozoic mélange

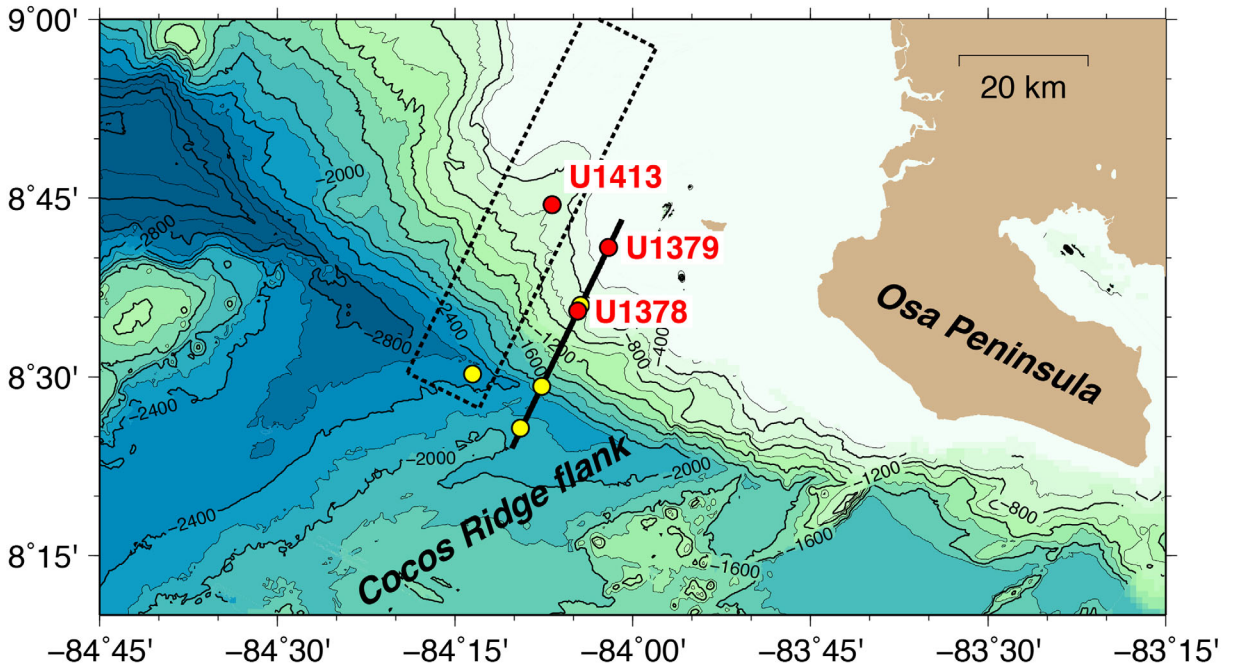

Figure 2. Sites drilled in the CRISP transect during IODP Expeditions 334 and 344, indicating the three sites where borehole breakouts were analyzed. The solid line shows the location of the cross section in Figure 3. The dotted line outlines the coverage of the 3-D seismic reflection survey of *Bangs et al*. [2015]. Bathymetry after *Weinrebe and Ranero* [2012], contour interval 200 m. The plot was generated with the Generic Mapping Tools (GMT) package [*Wessel et al*., 2013].

resulting from the accretion of oceanic seamounts [*Vannucchi et al*., 2006]. The Osa peninsula consists of a number of small (1–10 km) blocks bounded by subvertical faults that deform independently in response to the subduction of high-relief asperities on top of the underlying Cocos Ridge [*Vannucchi et al*., 2006; *Gardner et al*., 2013].

The three CRISP drill sites with breakout measurements are in the mid-slope (U1378) and upper slope (U1379 and U1413) of the convergent margin (Figure 2). On the upper slope, Site U1379 is located in locally flat topography whereas Site U1413 is above a bathymetric scar generated by the subduction of a seamount [*Kluesner et al*., 2013]. At the leading edge of the upper plate in the CRISP area, an approximately 5 km wide frontal prism of deformed sediment is immediately inland of the trench (Figure 3). The stratigraphy of the frontal prism is comparable to the stratigraphy of the incoming plate with a repetition of the sequence and age inversion, implying the presence of a thrust. Therefore, the frontal prism is an accretionary structure formed by sediments transferred from the incoming plate. Moving inboard across the margin, an apron of Recent to Pleistocene sediments up to ~1 km thick covers unconformably sediments of an

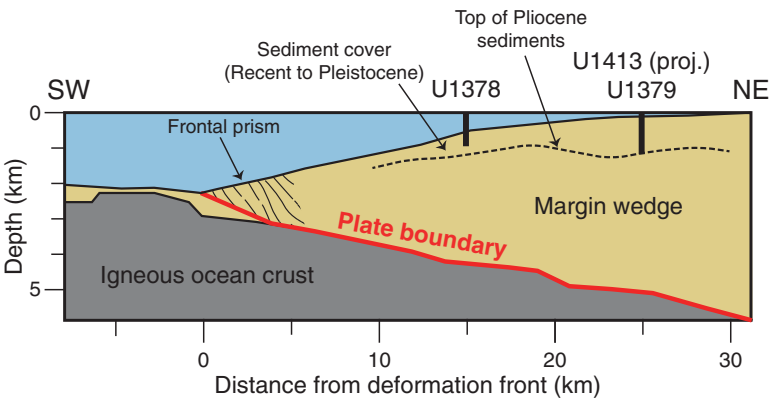

Figure 3. Schematic cross section through the CRISP drilling transect. Unit geometry after *Vannucchi et al*. [2012].

older, Pliocene, fore-arc basin [*Vannucchi et al*., 2012; *Harris et al*., 2013]. The three CRISP sites discussed here sampled the Recent to Pleistocene sediment cover; the older Pliocene sediments were reached by drilling only in the deepest portion of Site U1379 (below 895 m below seafloor, or mbsf).

Three-dimensional seismic reflection data have been acquired immediately to the NW of CRISP Sites U1378 and U1379, and Site U1413 was drilled in the area of seismic coverage (Figure 2). In the sediment cover, the seismic data show a pervasive pattern of small-displacement (tens of meters), closely spaced (∼200 m) normal faults [*Bangs et al*., 2015]. These normal faults form two sets, striking NNE-SSW and ENE-WSW. An additional set of E-W striking thrust faults, which tend to form along the crest of anticlinal ridges, is also present. Analyses of the cores obtained in CRISP drilling showed a variety of structures with predominant normal faults and strike-slip faults, typically concentrated in discrete horizons, and subordinate high-angle (dipping 70°–80°) reverse faults [*Vannucchi et al*., 2012; *Harris et al*., 2013].

The margin wedge beneath the sediment cover is characterized by three fault systems [*Bangs et al*., 2015]. Landward dipping thrusts are imaged beneath the lower slope, with few of them reaching the seafloor. Most of these thrust faults are associated to anticlines whose strike rotates from NE-SW to NW-SE moving from the trench to the top of the slope. Beneath the shelf break, a second NE-SW set of steep, seaward dipping thrust faults extend through all of the upper plate. This second set produced small offset across some of the normal faults that have formed within the overlying slope cover. The inner part of the wedge has a third set of landward dipping faults similar to the first one beneath the slope. The occurrence of a folded layered sequence in the margin wedge suggests that it is composed of deformed sediments rather than igneous rocks [*Bangs et al*., 2015].

The 2002 Osa Earthquake occurred near the plate boundary fault at a depth of ∼6 km and its epicenter has been located near IODP Site U1413 [*Arroyo et al*., 2014b]. This and other large earthquakes near the Osa peninsula (magnitude 6.4–7.4) have thrust focal mechanisms with a compressional axis parallel to the Cocos-Caribbean plate convergence (∼N30E). An analysis of recent seismicity in the area shows that the updip limit of the seismogenic zone becomes shallower moving from the NW to the SE toward the Osa peninsula [*Arroyo et al*., 2014a]. In the 3-D seismic data, the distribution of seismicity correlates with a shallowing of the boundary between an updip reflective plate boundary to a downdip weak reflection. This change in reflectivity has been interpreted to mark the transition between a fluid-rich and a well-drained subduction thrust [*Bangs et al*., 2015]. Almost all the seismic events mapped by *Arroyo et al*. [2014a] occur near the plate boundary fault or within the subducting slab, and they do not provide information on the state of stress within the margin wedge.

3. Horizontal Principal Stress Orientation and Borehole Breakouts

One of the principal stresses is perpendicular to the free boundary of the Earth surface, and we follow here the common assumption that the principal stress field in the subsurface lies in approximately vertical and horizontal planes [*Zoback*, 1992; *Bell*, 1996; *Zoback et al*., 2003]. With this assumption, the three principal stresses are a vertical stress S_V (given by the weight of the overburden) and two horizontal principal stresses, S_{Hmax} and S_{hmin} (Figure 4). Drilling a vertical borehole through a rock mass that is under different horizontal principal stresses induces a circumferential hoop stress along the borehole wall. This hoop stress depends on the difference $S_{Hmax} - S_{hmin}$ and reaches a maximum at the azimuth of the minimum horizontal stress. If the hoop stress exceeds the compressional rock strength, the borehole wall will fail developing characteristic breakouts located on opposite sides of the hole. These borehole breakouts mark the minimum horizontal stress direction and are key indicators of the state of stress in the subsurface [*Zoback et al*., 2003].

Wireline logging measurements can indicate the presence and measure the azimuth of borehole breakouts from the orientation of the arms in caliper tools and from borehole imaging. During IODP Exp. 344, a four-arm caliper tool was deployed to measure high-resolution electrical resistivity images of the borehole wall [*Ekstrom et al*., 1987]. The resistivity measurements are acquired by four pads on orthogonal arms that are pressed against the borehole wall during the recording. Each pad contains 16 button electrodes that measure a high-resolution resistivity image. The tool also records the aperture of each pair of caliper arms and their orientation with respect to magnetic north. Due to cable torque, this kind of caliper tool rotates while it is being pulled uphole. If breakouts are present, a pair of caliper arms will tend to remain within the breakout, stopping tool rotation. The breakout direction can then be determined from the orientation of the pair

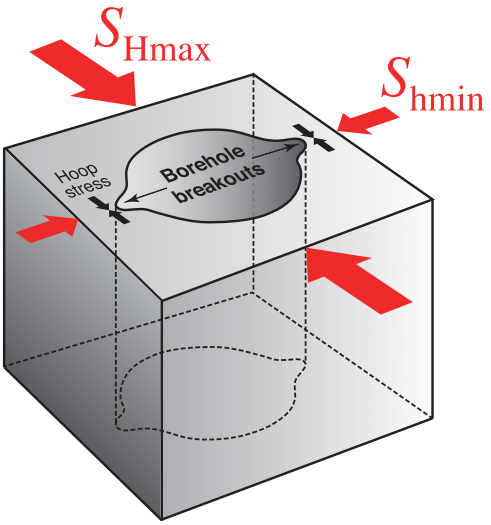

Figure 4. Relationship between orientation of borehole breakouts and of minimum and maximum principal horizontal stress directions (S_{hmin} and S_{Hmax}, respectively). Breakouts form if the compressional hoop stress on the borehole wall, which is maximum at the S_{hmin} azimuth, overcomes the rock strength.

of caliper arms that measures the larger borehole diameter [*Bell and Gough*, 1979; *Plumb and Hickman*, 1985; *Lin et al*., 2010].

IODP Exp. 344 also used a ultrasonic borehole televiewer [*Zemanek et al*., 1970]. In this tool, a rotating transducer emits ultrasonic pulses that are reflected by the borehole wall and then received by the same transducer. The continuous rotation of the transducer and the upward motion of the tool produce a complete image of the borehole wall. The borehole televiewer measures both the amplitude and travel time of the reflected ultrasonic pulse. The amplitude is mostly affected by the roughness of the borehole wall, with an additional minor contribution due to the contrast in acoustic impedance between the formation and the borehole fluid. In the amplitude images, the rough breakout surfaces show up as persistent vertical stripes of low reflectivity 180° apart. Measured travel times are converted to hole radius and provide detailed cross sections of the borehole that show the width and depth of breakouts [*Plumb and Hickman*, 1985; *Zoback et al*., 2003].

Azimuthal measurements acquired by logging-while-drilling (LWD) can also display borehole breakouts. Borehole breakouts are clearly seen in full coverage, high-resolution LWD resistivity images [*Chang et al*., 2010]. LWD resistivity images were not successfully collected during IODP Exp. 334, but the data acquired included azimuthal caliper measurements from ultrasonic travel times and from a gamma-gamma density log. The azimuthal density caliper measurements are based on the differences in density determined by the near and far detectors, which have different sensitivities to the standoff between the tool and the borehole [*Labat et al*., 2002]. The LWD tools used in IODP Exp. 334 measured borehole radius in 16 sectors, and further data processing was necessary to obtain reliable estimates of breakout azimuth, as described in the next section. More details on downhole log measurements acquired during IODP Expeditions 334 and 344 are in the IODP Proceedings [*Vannucchi et al*., 2012; *Harris et al*., 2013].

4. Results

4.1. Sites U1378 and U1379, IODP Exp. 334 (LWD Data)

The LWD data used to measure breakout orientations consist of azimuthal borehole radii measured by the density tool in 16 sectors (i.e., every 22.5°). To obtain detailed breakout orientations with an angular resolution better than that of the borehole radius measurements, we fitted to the data an ideal borehole shape consisting of the outer edge of a circle and a concentric ellipse (Figure 5). The azimuth of the fitted major axis of the ellipse defines the breakout orientation, whereas the length of the ellipse axes compared to the radius of the circle give the breakout depth and angle (the angular aperture of the inferred breakout). To estimate the uncertainty of the inferred breakout geometry, we applied a Markov chain Monte Carlo method where the parameters describing the borehole geometry (circle radius, ellipse orientation, and axis length) were iteratively perturbed following a random walk. The perturbed values were then accepted or rejected depending on how closely they fit the azimuthal borehole radius measurements following the Metropolis algorithm [*Metropolis et al*., 1953; *Chib and Greenberg*, 1995]. Example applications of the Metropolis algorithm to geophysical inverse problems are given by *Sen and Stoffa* [1995], *Sambridge and Mosegaard* [2002], and *Malinverno and Briggs* [2004]. In practice, this Monte Carlo procedure returns a large sample of borehole geometry parameters that fit the data. The sampled borehole geometry parameters are converted to breakout geometry parameters (breakout azimuth, depth, and angle). The average of the sampled breakout parameters gives best estimates and the sample variance measures their uncertainty given the data.

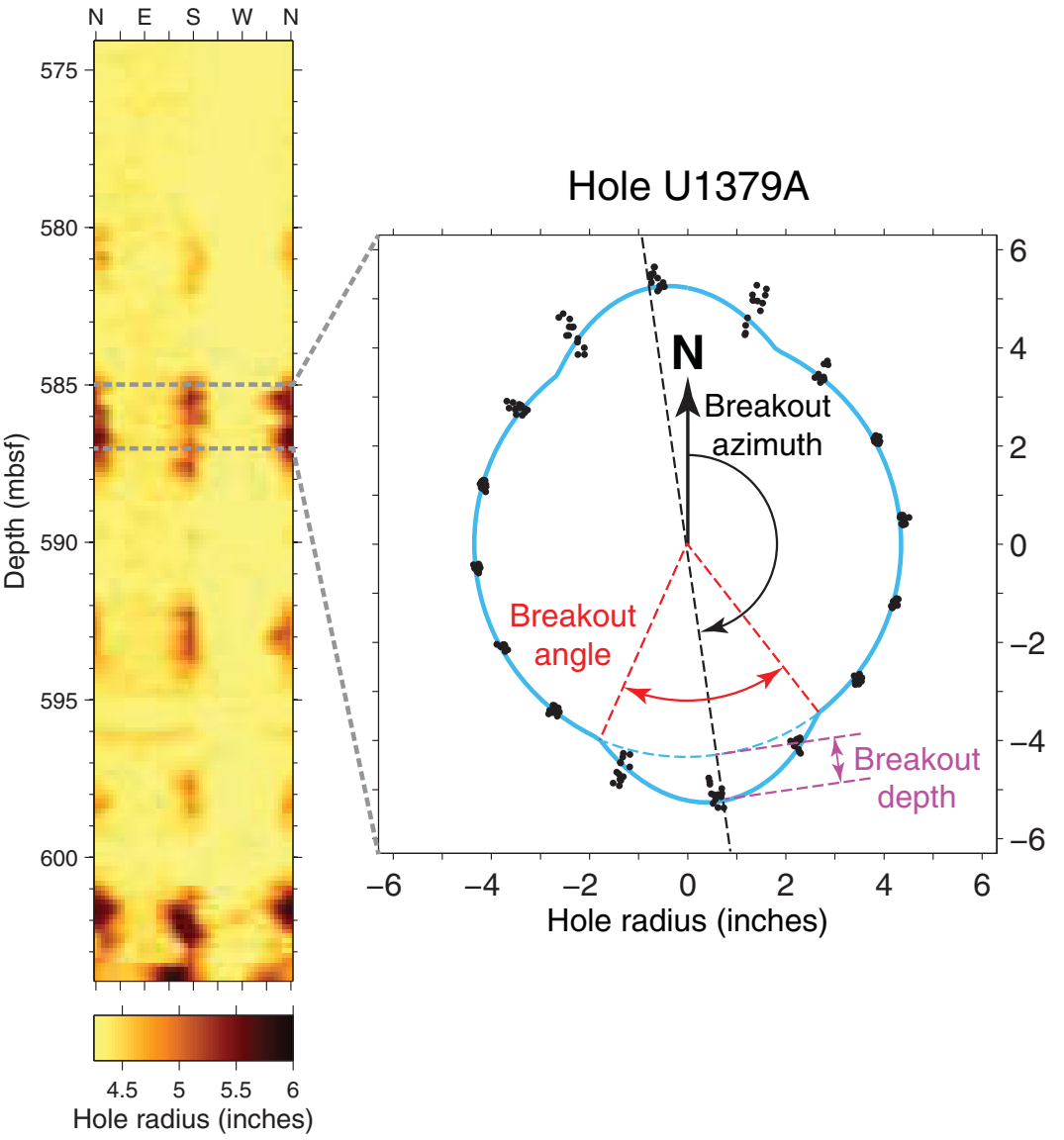

Figure 5. Breakout geometry parameters (azimuth, depth, and angle) are estimated by fitting an idealized borehole shape (the outer boundary of a concentric circle and ellipse) to LWD measurements of the borehole radius collected in a 2 m thick interval (black dots).

The breakout parameter uncertainties determined in the Monte Carlo sampling were used to decide which estimates of breakout geometry were reliable. This step was applied to avoid interpreting as breakouts borehole irregularities caused by other factors, such as an oval-shaped borehole due to drill string abrasion [*Plumb and Hickman*, 1985; *Yassir and Zerwer*, 1997]. The breakout geometry estimates were deemed valid if

1. The breakout azimuth was well defined (standard deviation $< 5°$);
2. The breakout depth was significant (estimated depth $>$ twice the standard deviation of breakout depth);
3. The breakout angle was not too large (estimated angle $< 180°$ minus twice the standard deviation of breakout angle); this requirement avoids detecting breakouts where the hole is elliptical.

The results of this analysis are in Figure 6. Reliable breakout orientations are consistently around ENE-WSW in the interval 200–440 mbsf of Site U1378. In most of the interval drilled at Site U1379 (300–865 mbsf), the breakouts are instead oriented approximately N-S. At the bottom of Site U1379 (865–895 mbsf), the breakout orientations rotate to about ESE-WNW. The change at 865 mbsf does not coincide with the bottom of the Recent to Pleistocene sedimentary apron, which was detected at 895 mbsf. The Pliocene fore-arc basin

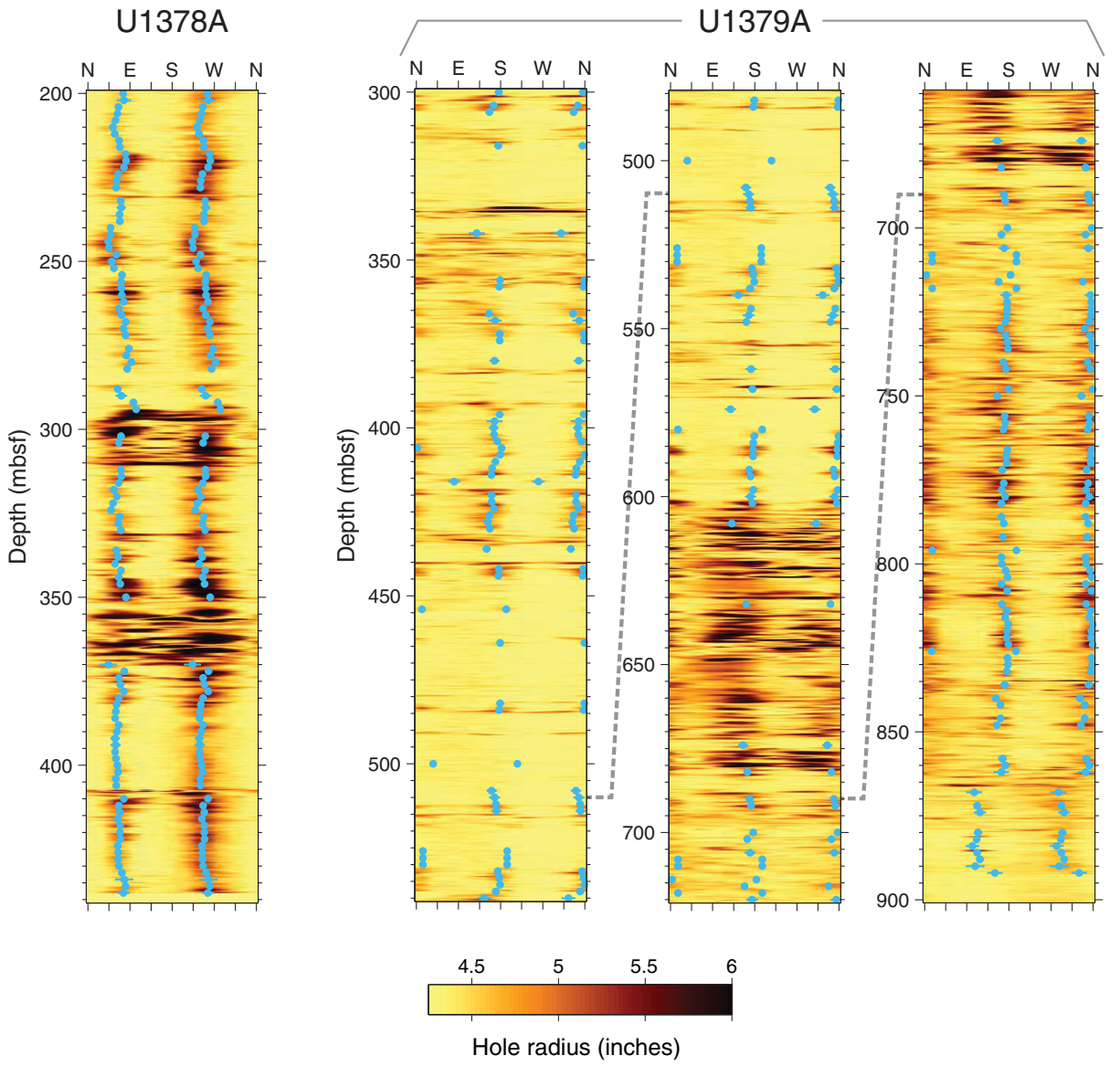

Figure 6. Estimated breakout azimuths in 2 m thick hole intervals (dots) and borehole radius images from LWD density measurements in Sites U1378 and U1379. Uncertainties in borehole azimuth (±two standard deviations) are shown as horizontal lines; in most cases, uncertainties are smaller than the size of the plotted dot. The three images on the right span the total interval with breakouts in U1379, and the dashed lines connect points at the same depth.

sediments below this depth have markedly greater bulk density and resistivity than those in the overlying younger sediment cover [*Vannucchi et al.*, 2012]. The approximately 50 m thick interval logged in the Pliocene sediments does not display any breakouts, likely because the formation is stronger than the overlying sediments and the hoop stress is insufficient to fracture it. Also, there was no clear evidence of breakouts in the shallower intervals drilled at these sites (above 200 mbsf in Site U1378 and above 300 mbsf in Site U1379).

4.2. Site U1413, IODP Exp. 344 (Wireline Log Data)

During IODP Exp. 344, wireline log measurements for breakout detection were successfully acquired in the interval 95–185 mbsf of Site U1413 (Figure 7). The two pairs of arms on the resistivity imaging tool measured significantly different borehole diameters in the interval 95–148 mbsf (Figures 7a and 7b). In this depth interval, the resistivity images recorded by pads on the caliper arms that measured the greater hole diameter display lower resistivities (darker image colors in Figure 7c). These observations suggest that a pair of

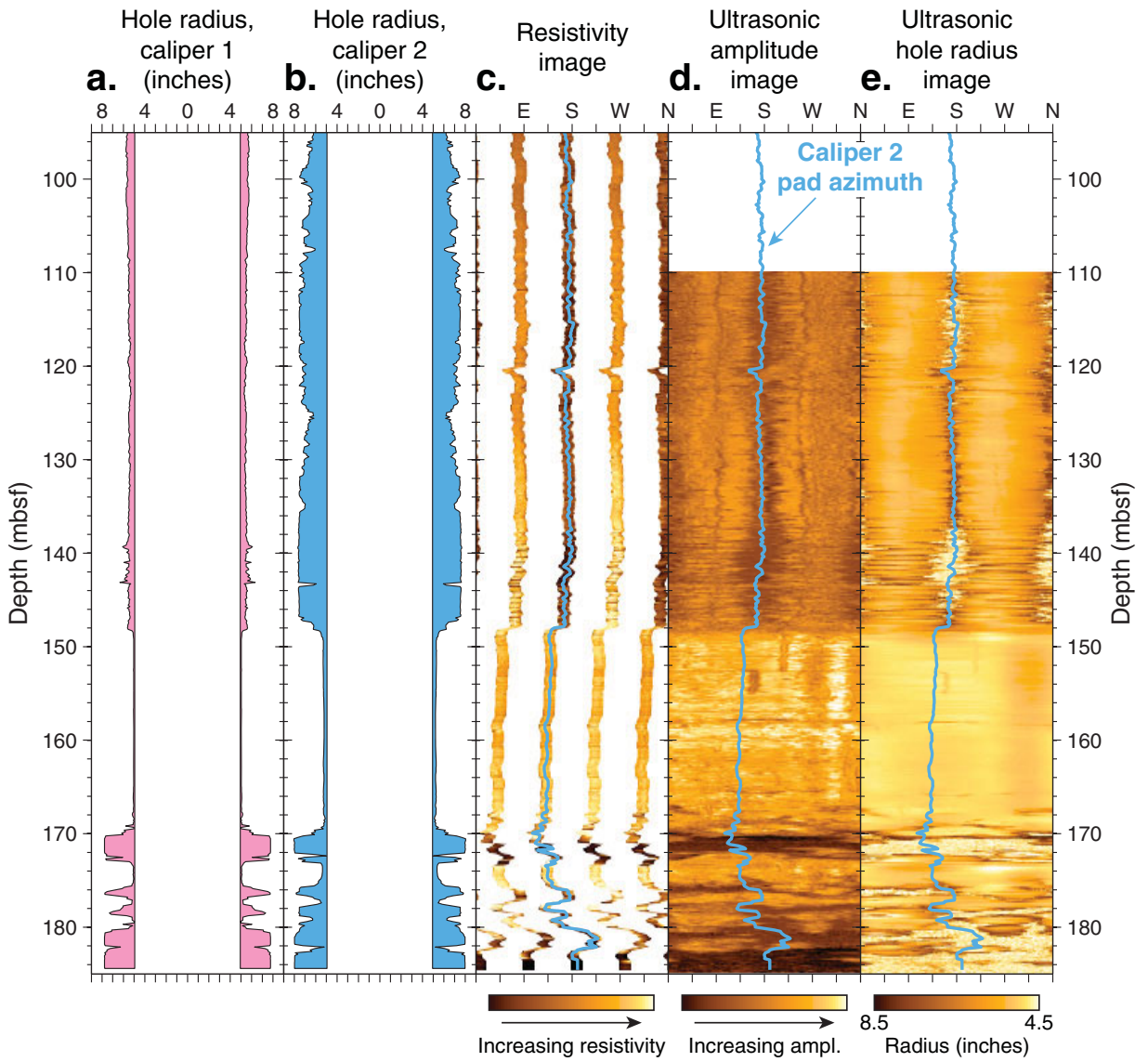

Figure 7. Breakout-related wireline log measurements in Site U1413. The borehole diameters measured by the two pairs of caliper arms on the resistivity imaging tool are in Figures 7a and 7b. The resistivity image is in Figure 7c and images with the amplitude and hole radius measured by the ultrasonic televiewer tool are in Figures 7d and 7e. The azimuth of the caliper arms that show the greater borehole diameter in the interval 95–148 mbsf is also shown in Figures 7c–7e.

caliper arms was stuck in breakouts during recovery, recording low resistivities because of poor pad contact along the rough borehole wall.

This interpretation is confirmed by the ultrasonic borehole televiewer measurements of reflection amplitude and borehole radius (Figures 7d and 7e, respectively). Ultrasonic reflection amplitudes are relatively low (as expected if the borehole wall is rough) and the borehole radius is larger at the azimuth of the caliper arms that measured the greater hole diameter.

The breakout orientation in the interval 95–148 mbsf can be estimated directly from the azimuth of the caliper arms that measured the greater hole diameter, and is approximately N-S. The rest of the logged interval at Site U1413 does not display breakouts. The caliper arms of the resistivity imaging tool and the ultrasonic borehole radius show a circular hole in the interval 148–170 mbsf. As noted at the base of Site U1379, the absence of breakouts in the 148–170 mbsf interval is likely due to a more compacted and stronger formation that did not fracture due to the hoop stress induced by differences between the horizontal principal stresses. Below 170 mbsf, the borehole becomes very irregular and the hole enlargements do not show a consistent orientation.

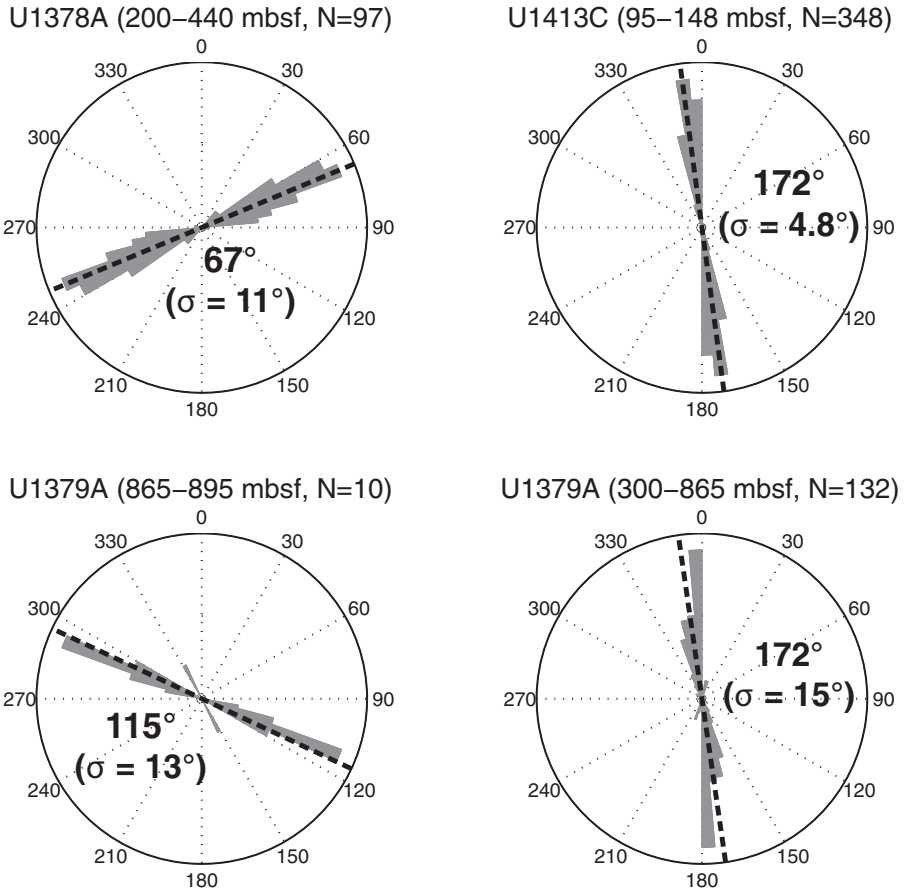

Figure 8. Circular histograms of breakout azimuths measured at Sites U1378, U1379, and U1413. Averages of measured breakout azimuths are plotted as thick dashed lines. Labels show the average and standard deviation (σ) of the breakout azimuths measured in each interval.

4.3. Breakout Azimuth Summary

Estimates of breakout azimuths are summarized in Figure 8, and data files with the values plotted in Figures 6–8 are provided in the supporting information. In Sites U1378 and U1413, breakout directions are consistent within the entire depth interval where they were observed, but they clearly differ above and below 865 mbsf at Site U1379. There are essentially three sets of breakout azimuths in our data set. The deepest interval with breakouts in Site U1379 (865–895 mbsf) has an average breakout azimuth of 115° with a standard deviation (σ) of 13°. Breakouts measured above 895 mbsf in Site U1379 and in Site U1413 have the same average orientation of 172° ($\sigma = 15°$ and 4.8°, respectively). Finally, Site U1378 displays an average breakout direction of 67° ($\sigma = 11°$), which is almost perpendicular to that observed in the shallower portion of Site U1379 and in Site U1413. These three sets have relatively small standard deviations and are clearly statistically different.

5. Discussion

The orientations of the maximum horizontal principal stresses S_{Hmax}, which are perpendicular to the breakout azimuths, are plotted in Figure 9. There are three overall S_{Hmax} orientations: NNE-SSW (25° azimuth) in Site U1379 below 865 mbsf; ENE-WSW (82°) in Site U1413 and Site U1379 above 865 mbsf; and NNW-SSE (157°) in Site U1378. To explain the observed variation in stress orientation, consider the two end-members described by *Bell* [1996] for the state of stress in sedimentary sequences. If sediments rest directly on and are mechanically coupled to a deeper unit, the principal stress directions in the sediments will record the signature of the underlying rocks and generally will be spatially uniform. In contrast, if there are intermediate zones of geomechanical weakness such as low strength rocks or fault zones, the sediments will be

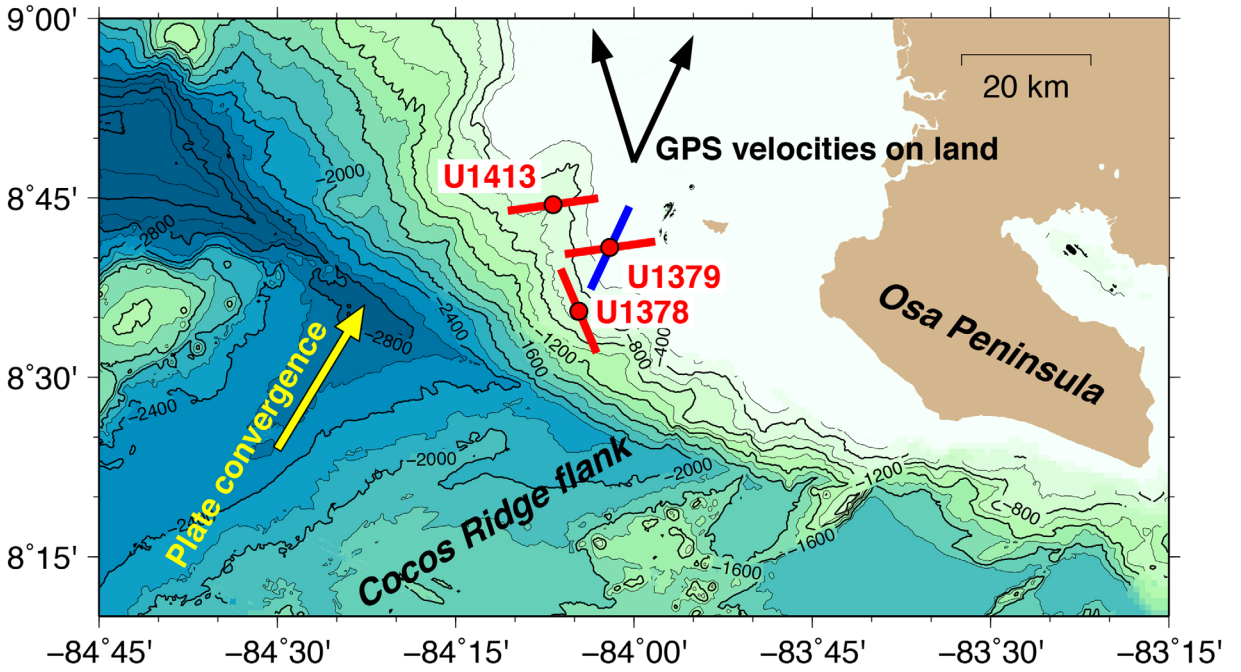

Figure 9. S_{Hmax} orientations in three CRISP sites. The blue line segment indicates the S_{Hmax} direction measured below 865 mbsf in Site U1379; the red line segments show the S_{Hmax} direction at depths above 865 mbsf in Site U1379 and in the whole depth interval where breakouts were detected in Sites U1378 and U1413. The yellow arrow denotes the Cocos-Caribbean plate relative motion. The black arrows span the range of GPS velocity directions measured with respect to the Caribbean plate on the Costa Rica mainland NW of the Osa peninsula [*LaFemina et al.*, 2009]. Bathymetry after *Weinrebe and Ranero* [2012], contour interval 200 m. The plot was generated with the Generic Mapping Tools (GMT) package [*Wessel et al.*, 2013].

mechanically detached from the deeper units and principal stress directions will typically vary over short distances. Faults that dissect the sediment sequence can cause some of this spatial variability, because one of the principal stresses will rotate to become locally perpendicular to a mechanically weak fault [*Bell*, 1996; *Yassir and Zerwer*, 1997].

S_{Hmax} near the base of the sediment cover in Site U1379 (865–895 mbsf) is oriented in the same direction as the Cocos-Caribbean plate convergence (Figure 9) and the compression direction of thrust earthquakes that occur near the plate boundary fault. The stress state in the upper plate of a convergent margin is controlled by the balance between gravitational force, which promotes margin-perpendicular extension, and shear force along the plate boundary fault, which induces compression [*Wang and He*, 1999; *Wang et al.*, 2010]. The S_{Hmax} direction in the 865–895 mbsf interval of Site U1379 may therefore correspond to a compressional state of stress in the margin wedge. This interpretation agrees with observations in Nankai Trough Site C0009, where the S_{Hmax} directions are not constant in the entire drilled interval but rotate in the deeper borehole section, where they become nearly parallel to the direction of plate convergence [*Lin et al.*, 2010].

The change in S_{Hmax} azimuth at 865 mbsf in Site U1379 coincides with a marked increase in deformation features in the cores and with fluid chemistry anomalies [*Vannucchi et al.*, 2012], and it could be related to a fault. A fault zone near the base of the sediment cover would mechanically detach the sediments from the deeper margin wedge, and the principal stress directions could be dominantly controlled by the pattern of normal faults in the sediment cover. Decoupling of the sediment cover from the deep stress field is also supported by the observation that the S_{Hmax} azimuth in U1413 is the same as that above 865 mbsf in U1379, although the stress field beneath U1413 should be affected by the subduction of a seamount [*Kluesner et al.*, 2013]. If a network of faults with different orientations dissects the sediment cover in a number of separate blocks, principal stress directions can be different in different blocks and may rotate near faults within a block. In the CRISP area, 3-D seismic reflection images show a network of closely spaced normal faults in the sediment cover [*Bangs et al.*, 2015]. Geological mapping of the Osa peninsula detected two orthogonal sets of normal faults striking NW-SE and NE-SW [*Vannucchi et al.*, 2006]. The strikes of these

faults are close to the S_{Hmax} directions in Site U1378 (NNW-SSE) and in Sites U1413 and U1379 above 865 mbsf (ENE-WSW).

The simplest interpretation of our results is that the deeper interval of the sediment cover in Site U1379 records the compressional state of stress in the underlying margin wedge, whereas the variable stress directions observed elsewhere are controlled by a network of normal faults in the sediment cover.

The principal stress directions may also be affected by other factors. The subducting Cocos Ridge has been proposed to act as an indenter, as shown by a margin-parallel component of fore-arc deformation measured on Costa Rica GPS land stations [*LaFemina et al*., 2009; *Kobayashi et al*., 2014]. With the exception of the deepest interval in Site U1379, the S_{Hmax} directions we observe are approximately parallel and perpendicular to the isobaths of the Cocos Ridge flank and to the most westerly azimuths of the GPS velocities in the land area NW of the Osa peninsula (Figure 9). In principle, the subduction of the Cocos Ridge adjacent to the CRISP sites could cause a counterclockwise rotation of the horizontal principal stresses in the upper plate from the direction of plate convergence. On the other hand, S_{Hmax} in the deeper interval of Site U1379, which should record more closely the state of stress at depth, is parallel to the plate convergence vector and does not seem to be affected by the Cocos Ridge indentation.

The change in S_{Hmax} direction between Sites U1378 and U1379 also coincides with the transition projected to the SE of the 3-D seismic volume between high and low reflectivity on the plate boundary fault, which has been related to the presence of overpressured fluids [see *Bangs et al*., 2015, Figure 12]. The updip limit of the seismogenic zone is also approximately located between Sites U1378 and U1379 [see *Arroyo et al*., 2014a, Figure 1]. A change in the coupling of the plate boundary fault could result in different states of stress in the upper plate. However, there does not seem to be a straightforward relationship with the S_{Hmax} directions we measure in the sediment cover, as they are mostly oblique to the plate convergence and to the compressional direction of subduction earthquakes.

Our conclusions are based only on the orientations of the principal horizontal stresses, and are necessarily limited. To characterize fully the subsurface state of stress, the magnitudes of the principal stress are needed besides their direction, and can be estimated from rock deformation data [*Chang et al*., 2010]. On the basis of the S_{Hmax} orientation and uniaxial compressional strength tests, *Saito et al*. [2013] suggest that the CRISP upper slope sites (U1379 and U1413) are in a normal fault regime and the mid-slope site (U1378) is in a strike-slip regime. Further work will use the S_{Hmax} orientations discussed here to characterize more fully the present state of stress in the CRISP transect.

6. Conclusions

Borehole breakout orientations obtained from wireline and LWD logs collected during CRISP drilling show three overall orientations of the maximum principal horizontal stress S_{Hmax}: NNE-SSW (25° azimuth) in the deepest interval drilled at the upper slope Site U1379 (865–895 mbsf); ENE-WSW (82°) in the rest of Site U1379 and in Site U1413, also drilled in the upper slope; and NNW-SSE (157°) in the mid-slope Site U1378. All these measurements of S_{Hmax} were obtained in the Recent to Pleistocene sediment cover of the CRISP margin, above the deeper rocks of the deformed margin wedge.

Our preferred interpretation of these results is that the deepest interval of Site U1379 records the stress conditions in the underlying margin wedge, as S_{Hmax} is oriented in the same direction of the Cocos-Caribbean plate convergence and of the compressional axes of thrust earthquakes that occur along the plate boundary fault. The approximately orthogonal S_{Hmax} directions observed in the other intervals are likely due to the effect of a network of normal faults that subdivide the sediment cover into a number of independently deforming blocks. Principal stresses are expected to rotate near low-strength faults, resulting in spatially variable S_{Hmax} directions. In addition, the maximum principal horizontal stress directions may be influenced by the indenting Cocos Ridge, which causes a counterclockwise rotation of deformation vectors, and by the transition between aseismic and seismogenic subduction along the plate boundary fault.

Acknowledgments
This research used samples and data provided by the Integrated Ocean Drilling Program (IODP). The efforts of the JOIDES Resolution shipboard and drilling personnel and of the scientific party of IODP Expeditions 334 and 344 are gratefully acknowledged. We also thank two anonymous reviewers for constructive comments that improved the paper. A.M. was supported by the U.S. Science Support Program (awards T334A34 and T344B34). Files with the data used in this paper (breakout azimuth estimates in Figures 6–8) are provided in the supporting information. This is L-DEO contribution number 7957.

References

Arroyo, I. G., S. Husen, and E. R. Flueh (2014a), The seismogenic zone in the Central Costa Rican Pacific margin: High-quality hypocentres from an amphibious network, *Int. J. Earth Sci.*, *103*, 1747–1764, doi:10.1007/s00531-013-0955-8.

Arroyo, I. G., I. Grevemeyer, C. R. Ranero, and R. von Huene (2014b), Interplate seismicity at the CRISP drilling site: The 2002 Mw 6.4 Osa Earthquake at the southeastern end of the Middle America Trench, *Geochem. Geophys. Geosyst.*, *15*, 3035–3050, doi:10.1002/2014GC005359.

Bangs, N. L., K. D. McIntosh, E. A. Silver, J. W. Kluesner, and C. R. Ranero (2015), Fluid accumulation along the Costa Rica subduction thrust and development of the seismogenic zone: The Costa Rica subduction thrust and development of the seismogenic zone, *J. Geophys. Res. Solid Earth*, *120*, 67–86, doi:10.1002/2014JB011265.

Bell, J. S. (1996), In situ stresses in sedimentary rocks (part 2): Applications of stress measurements, *Geosci. Can.*, *23*, 135–153.

Bell, J. S., and D. I. Gough (1979), Northeast-southwest compressive stress in Alberta: Evidence from oil wells, *Earth Planet. Sci. Lett.*, *45*, 475–482.

Chang, C., L. C. McNeill, J. C. Moore, W. Lin, M. Conin, and Y. Yamada (2010), In situ stress state in the Nankai accretionary wedge estimated from borehole wall failures, *Geochem. Geophys. Geosyst.*, *11*, Q0AD04, doi:10.1029/2010GC003261.

Chib, S., and E. Greenberg (1995), Understanding the Metropolis-Hastings algorithm, *Am. Stat.*, *49*, 327–335.

Clift, P., and P. Vannucchi (2004), Controls on tectonic accretion versus erosion in subduction zones: Implications for the origin and recycling of the continental crust, *Rev. Geophys.*, *42*, RG2001, doi:10.1029/2003RG000127.

Ekstrom, M. P., C. Dahan, M.-Y. Chen, P. Lloyd, and D. J. Rossi (1987), Formation imaging with microelectrical scanning arrays, *Log Anal.*, *28*, 294–306.

Gardner, T. W., D. M. Fisher, K. D. Morell, and M. L. Cupper (2013), Upper-plate deformation in response to flat slab subduction inboard of the aseismic Cocos Ridge, Osa Peninsula, Costa Rica, *Lithosphere*, *5*, 247–264, doi:10.1130/L251.1.

Harris, R. N., A. Sakaguchi, K. E. Petronotis, and Expedition 344 Scientists (2013), *Proceedings of Integrated Ocean Drilling Program, Expedition 344*, Ocean Drill. Program, College Station, Tex.

Heidbach, O., M. Tingay, A. Barth, J. Reinecker, D. Kurfeß, and B. Müller (2009), *The World Stress Map Based on the Database Release 2008*, Comm. for the Geol. Map of the World, Paris, doi:10.1594/GFZ.WSM.Map2009.

Kluesner, J. W., E. A. Silver, J. Gibson, N. L. Bangs, K. D. McIntosh, D. Orange, C. R. Ranero, and R. von Huene (2013), High density of structurally controlled, shallow to deep water fluid seep indicators imaged offshore Costa Rica, *Geochem. Geophys. Geosyst.*, *14*, 519–539, doi:10.1002/ggge.20058.

Kobayashi, D., P. LaFemina, H. Geirsson, E. Chichaco, A. A. Abrego, H. Mora, and E. Camacho (2014), Kinematics of the western Caribbean: Collision of the Cocos Ridge and upper plate deformation, *Geochem. Geophys. Geosyst.*, *15*, 1671–1683, doi:10.1002/2014GC005234.

Labat, C., S. Brady, M. Everett, D. Ellis, M. Doghmi, J. C. Tomlinson, and G. Shehab (2002), 3D azimuthal LWD caliper, paper SPE 77526 presented at SPE Annual Technical Conference and Exhibition, Soc. of Pet. Eng., San Antonio.

LaFemina, P., T. H. Dixon, R. Govers, E. Norabuena, H. Turner, A. Saballos, G. Mattioli, M. Protti, and W. Strauch (2009), Fore-arc motion and Cocos Ridge collision in Central America, *Geochem. Geophys. Geosyst.*, *10*, Q05S14, doi:10.1029/2008GC002181.

Lin, W., et al. (2010), Present-day principal horizontal stress orientations in the Kumano forearc basin of the southwest Japan subduction zone determined from IODP NanTroSEIZE drilling Site C0009, *Geophys. Res. Lett.*, *37*, L13303, doi:10.1029/2010GL043158.

Malinverno, A., and V. A. Briggs (2004), Expanded uncertainty quantification in inverse problems: Hierarchical Bayes and empirical Bayes, *Geophysics*, *69*, 1005–1016, doi:10.1190/1.1778243.

Metropolis, N., A. W. Rosenbluth, M. N. Rosenbluth, A. H. Teller, and E. Teller (1953), Equation of state calculations by fast computing machines, *J. Chem. Phys.*, *21*, 1087–1092.

Plumb, R. A., and S. H. Hickman (1985), Stress-induced borehole elongation: A comparison between the four-arm dipmeter and the borehole televiewer in the Auburn geothermal well, *J. Geophys. Res.*, *90*, 5513–5521.

Saito, S., A. Malinverno, W. Lin, Y. Yamamoto, H. Wu, R. N. Harris, A. Sakaguchi, K. Ujiie, P. Vannucchi, and K. E. Petronotis (2013), Preliminary results on horizontal stress orientation and stress magnitude off Osa Peninsula, Costa Rica, Abstract T31G-2595 presented at 2013 Fall Meeting, AGU, San Francisco, Calif., 9–13 Dec.

Sambridge, M., and K. Mosegaard (2002), Monte Carlo methods in geophysical inverse problems, *Rev. Geophys.*, *40*(3), 1009, doi:10.1029/2000RG000089.

Sen, M. K., and P. L. Stoffa (1995), *Global Optimization Methods in Geophysical Inversion*, Elsevier, Amsterdam.

Tobin, H., P. Henry, P. Vannucchi, and E. Screaton (2014), Subduction Zones: Structure and Deformation History, in *Earth and Life Processes Discovered From Subseafloor Environment—A Decade of Science Achieved by the Integrated Ocean Drilling Program (IODP)*, edited by R. Stein et al., pp. 599–640, Elsevier, Amsterdam, doi:10.1016/B978-0-444-62617-2.00020-7.

Vannucchi, P., D. M. Fisher, T. W. Gardner, and S. Bier (2006), From seamount accretion to tectonic erosion: Formation of Osa Mélange and the effects of Cocos Ridge subduction in southern Costa Rica, *Tectonics*, *25*, TC2004, doi:10.1029/2005TC001855.

Vannucchi, P., K. Ujiie, N. Stroncik, A. Malinverno, and Expedition 334 Scientists (2012), *Proceedings of Integrated Ocean Drilling Program, Expedition 334*, Ocean Drill. Program, College Station, Tex.

Vannucchi, P., P. B. Sak, J. Phipps Morgan, K. Ohkushi, K. Ujiie, and IODP Expedition 334 Shipboard Scientists (2013), Rapid pulses of uplift, subsidence, and subduction erosion offshore Central America: Implications for building the rock record of convergent margins, *Geology*, *41*, 995–998, doi:10.1130/G34355.1.

von Huene, R., and D. W. Scholl (1991), Observations at convergent margins concerning sediment subduction, subduction erosion, and the growth of continental crust, *Rev. Geophys.*, *29*, 279–316.

Walther, C. H. E. (2003), The crustal structure of the Cocos ridge off Costa Rica, *J. Geophys. Res.*, *108*(B3), 2136, doi:10.1029/2001JB000888.

Wang, K., and J. He (1999), Mechanics of low-stress forearcs: Nankai and Cascadia, *J. Geophys. Res.*, *104*, 15,191–15,205, doi:10.1029/1999JB900103.

Wang, K., and Y. Hu (2006), Accretionary prisms in subduction earthquake cycles: The theory of dynamic Coulomb wedge, *J. Geophys. Res.*, *111*, B06410, doi:10.1029/2005JB004094.

Wang, K., Y. Hu, R. von Huene, and N. Kukowski (2010), Interplate earthquakes as a driver of shallow subduction erosion, *Geology*, *38*, 431–434, doi:10.1130/G30597.1.

Weinrebe, W., and C. R. Ranero (2012), Multibeam bathymetry compilation of the Central America Pacific Margin, Integrated Earth Data Alliance, doi:10.1594/IEDA/100069.

Wessel, P., W. H. F. Smith, R. Scharroo, J. Luis, and F. Wobbe (2013), Generic mapping tools: Improved version released, *Eos Trans. AGU*, *94*, 409–410.

Yassir, N. A., and A. Zerwer (1997), Stress regimes in the Gulf Coast, offshore Louisiana: Data from well-bore breakout analysis, *AAPG Bull.*, *81*, 293–307.

Zemanek, J., E. E. Glenn, L. J. Norton, and R. L. Caldwell (1970), Formation evaluation by inspection with the borehole televiewer, *Geophysics*, *35*, 254–269.

Zoback, M. D., C. A. Barton, M. Brudy, D. A. Castillo, T. Finkbeiner, B. R. Grollimund, D. B. Moos, P. Peska, C. D. Ward, and D. J. Wiprut (2003), Determination of stress orientation and magnitude in deep wells, *Int. J. Rock Mech. Min. Sci.*, *40*, 1049–1076, doi:10.1016/j.ijrmms.2003.07.001.

Zoback, M. L. (1992), First- and second-order patterns of stress in the lithosphere: The World Stress Map project, *J. Geophys. Res.*, *97*, 11,703–11,728.